Journal of The Electrochemical Society, **155** (7) H545-H551 (2008)
0013-4651/2008/155(7)/H545/7/$23.00 © The Electrochemical Society

Nanoindentation Investigation of HfO_2 and Al_2O_3 Films Grown by Atomic Layer Deposition

K. Tapily,[a,c,*] J. E. Jakes,[d,e] D. S. Stone,[d,e] P. Shrestha,[a,c,*] D. Gu,[a,c,,z] H. Baumgart,[a,c,**] and A. A. Elmustafa[b,c]**

[a]*Department of Electrical Engineering and* [b]*Department of Mechanical Engineering, Old Dominion University, Norfolk, Virginia 23529, USA*
[c]*Thomas Jefferson Laboratory, Applied Research Center, Newport News, Virginia 23606, USA*
[d]*Department of Materials Science and Engineering, University of Wisconsin-Madison, Madison, Wisconsin 53706, USA*
[e]*United States Department of Agriculture Forest Products Laboratory, Madison, Wisconsin 53726, USA*

The challenges of reducing gate leakage current and dielectric breakdown beyond the 45 nm technology node have shifted engineers' attention from the traditional and proven dielectric SiO_2 to materials of higher dielectric constant also known as high-k materials such as hafnium oxide (HfO_2) and aluminum oxide (Al_2O_3). These high-k materials are projected to replace silicon oxide (SiO_2). In order to address the complex process integration and reliability issues, it is important to investigate the mechanical properties of these dielectric materials in addition to their electrical properties. In this study, HfO_2 and Al_2O_3 have been fabricated using atomic layer deposition (ALD) on (100) p-type Si wafers. Using nanoindentation and the continuous stiffness method, we report the elastomechanical properties of HfO_2 and Al_2O_3 on Si. ALD HfO_2 thin films were measured to have a hardness of 9.5 ± 2 GPa and a modulus of 220 ± 40 GPa, whereas the ALD Al_2O_3 thin films have a hardness of 10.5 ± 2 GPa and a modulus of 220 ± 40 GPa. The two materials are also distinguished by very different interface properties. HfO_2 forms a hafnium silicate interlayer, which influences its nanoindentation properties close to the interface with the Si substrate, while Al_2O_3 does not exhibit any interlayer.
 [DOI: 10.1149/1.2919106]

Manuscript submitted January 14, 2008; revised manuscript received March 24, 2008. Available electronically May 20, 2008.

For the past 40 years the microelectronics industry has relied on the scaling down of device size in order to improve the performance, functionality, and bit density of chips, as described by Moore's law. As microelectronics is transitioning into deep nanotechnology, the drawback of the increasing miniaturization of devices is the increase of gate leakage current and oxide breakdown.[1] To reduce the gate leakage current and breakdown field across the gate insulator, researchers are looking into high-k dielectric materials. High-k materials such as HfO_2 and Al_2O_3 will increase the transistor drive current and the transistor switching speed.[2] HfO_2 is predicted to replace SiO_2, SiO_xN_y, and Si_3N_4 as the gate dielectric of complementary metal oxide semiconductor (CMOS) devices at the 45 nm technology node and beyond. HfO_2 and Al_2O_3 have dielectric constants of approximately $k = 25$ and 8, respectively,[3] which compare favorably with $k = 3.9$ for SiO_2. Various deposition techniques have been used to deposit high-k materials. Among these growth techniques are metallorganic chemical vapor deposition (MOCVD),[4-6] pulsed laser deposition (PLD),[7] and atomic layer deposition (ALD).[4-6,8] MOCVD and PLD require a high temperature during processing and film fabrication.[9] For example, a minimum temperature of 600°C is required to deposit HfO_2 with MOCVD, whereas HfO_2 crystallizes once the temperature reaches 600°C.[10] ALD is a chemical reaction-based deposition technique that requires only relatively low temperatures. ALD provides absolute film deposition uniformity (atomic layer by atomic layer), precise composition control, high conformality, and completely self-limiting surface reactions, which makes ALD the most suitable low-temperature high-k dielectric materials' deposition technique for coating of complex surface topographies in nanoelectronic applications.

ALD also provides the user better control over the deposition parameters.[8] Each chemical reaction that takes place in an ALD reactor is self-limiting, meaning a given reactant will not react further than surface saturation in a given pulse, even if the exposure with the chemical precursor is continued for a long time. The reaction by-products are purged out with an inert gas, typically N_2 or Ar. Another trait that uniquely defines ALD as the most appropriate technique to deposit high-k dielectric nanoelectronic materials is the high aspect ratio of the films deposited, which is important for today's complex surface topographies. In fact, ALD deposits an accurate film thickness and offers a large area uniformity. The final thickness of ALD films depends on the number of ALD deposition cycles used. In an ALD cycle, chemical precursors are pulsed and purged consecutively until all precursors are reacted and deposited.

The electrical properties of high-k dielectric materials such as HfO_2 and Al_2O_3 have been widely studied and investigated. However, little is known about their mechanical properties. The nanomechanical properties of high-k dielectrics are of great technological importance because the elastomechanical response to thermal cycling and process-induced stress has an effect on the process integration compatibility and long-term reliability. Nanoindentation is widely used as a testing mechanism for hardness, modulus, and fracture toughness of thin films.[11-13] In this paper, we use nanoindentation testing techniques and atomic force microscopy (AFM) imaging of the indentation impressions to investigate the mechanical properties such as modulus and hardness of HfO_2 and Al_2O_3 thin films.

Sample Fabrication

We deposited 60, 30, and 10 nm films of HfO_2 by ALD on (100) Si substrates using identical deposition conditions for each film. Similar film thicknesses of Al_2O_3 were also deposited. Tetrakisdimethylamidohafnium IV (TDMAH) and trimethylaluminum (TMA) were used as chemical precursors for HfO_2 and Al_2O_3, respectively, for these reactions. H_2O vapor was the oxidation source for the reactions. For HfO_2 deposition, the TDMAH precursor tank was heated at 75°C prior to deposition. The deposition cycle consisted of pulsing TDMAH, purging N_2, and pulsing H_2O vapor. Film deposition parameters such as flow rate, pulse time, pump time, exposure, and delay time were maintained fixed. For example, the HfO_2 films were deposited at 250°C whereas Al_2O_3 films were deposited on the Si substrates at 300°C. The chamber pressure was 2.1×10^{-1} Torr for both HfO_2 and Al_2O_3. For each ALD growth cycle the oxidizing agent in the form of water vapor (H_2O) was pulsed for 25 ms and the TDMAH and TMA precursors were each pulsed for 1 s duration. Al_2O_3 was deposited under similar conditions as in HfO_2. The cycle consisted of pulsing TMA, purging N_2, and pulsing H_2O. However, in this case the TMA precursor tank was not heated.

* Electrochemical Society Student Member.
** Electrochemical Society Active Member.
z E-mail: dgu@odu.edu

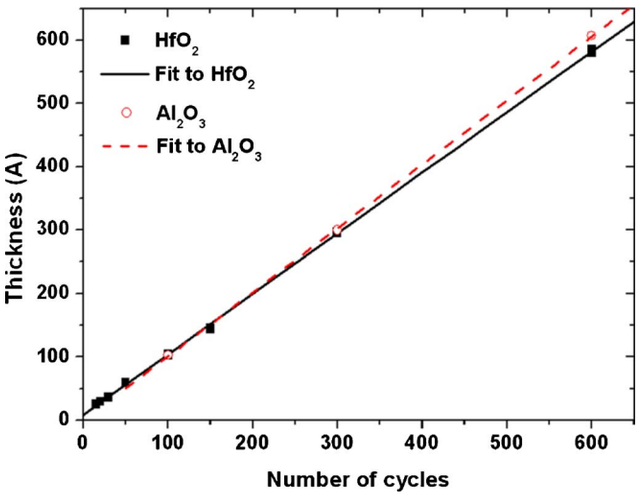

Figure 1. (Color online) Linearity of HfO_2 (black square) and Al_2O_3 (circle) film thickness with ALD cycles at 250°C. The film thicknesses were measured using the spectroscopic ellipsometer (Woollam, VASE).

The thickness vs the number of cycles for HfO_2 and Al_2O_3 is shown in Fig. 1. From the graph, one can see that the deposition rate is linear, which allowed us to predict the number of cycles necessary to deposit a desired film thickness. The thickness of the films was measured by a spectroscopic ellipsometer (Woollam, VASE). Table I summarizes the actual films' thickness subsequent to ALD deposition.

Transmission electron microscope (TEM) and AFM analysis were performed on a 4 nm HfO_2 sample to illustrate the uniformity and roughness of the films. A high-resolution TEM micrograph of HfO_2 film on bulk silicon is shown in Fig. 2. Note that the HfO_2 films deposited at 250°C are primarily amorphous, as depicted by the high-magnification TEM cross section in Fig. 2. These HfO_2 films also contain a number of crystallites, which are not shown in this TEM micrograph, but which are clearly evident from our AFM characterization. AFM analysis was performed in the tapping mode on the samples to examine the surface morphology in a scan area of 1×1 μm. The surface roughness of the Al_2O_3 samples was about 0.12 nm and almost constant for various thicknesses. In contrast, the surface roughness of HfO_2 increases as a function of the film thickness. A final root-mean-square (rms) surface roughness of 3.3 nm was observed for the 60 nm films. Such an increased surface roughness affects the nanoindentation measurements. ALD HfO_2 films deposited at 250°C were almost 30 times rougher than the Al_2O_3 films deposited at 300°C. A three-dimensional (3D) AFM image in Fig. 3 shows the 60 nm Al_2O_3 and the 60 nm HfO_2 films side by side.

Table I. Summary of the film thicknesses obtained by spectroscopic ellipsometry.

Thin film	Desired thickness (Å)	Measured thickness (Å)
HfO_2	600	583
HfO_2	300	296
HfO_2	100	104
Al_2O_3	600	607
Al_2O_3	300	300
Al_2O_3	100	103

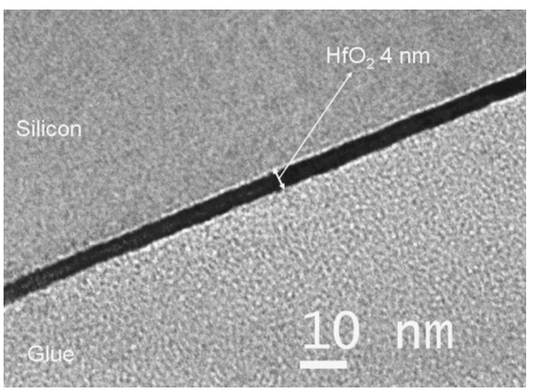

Figure 2. High-resolution TEM cross-section micrograph of a 4 nm HfO_2 film deposited by ALD on a Si substrate.

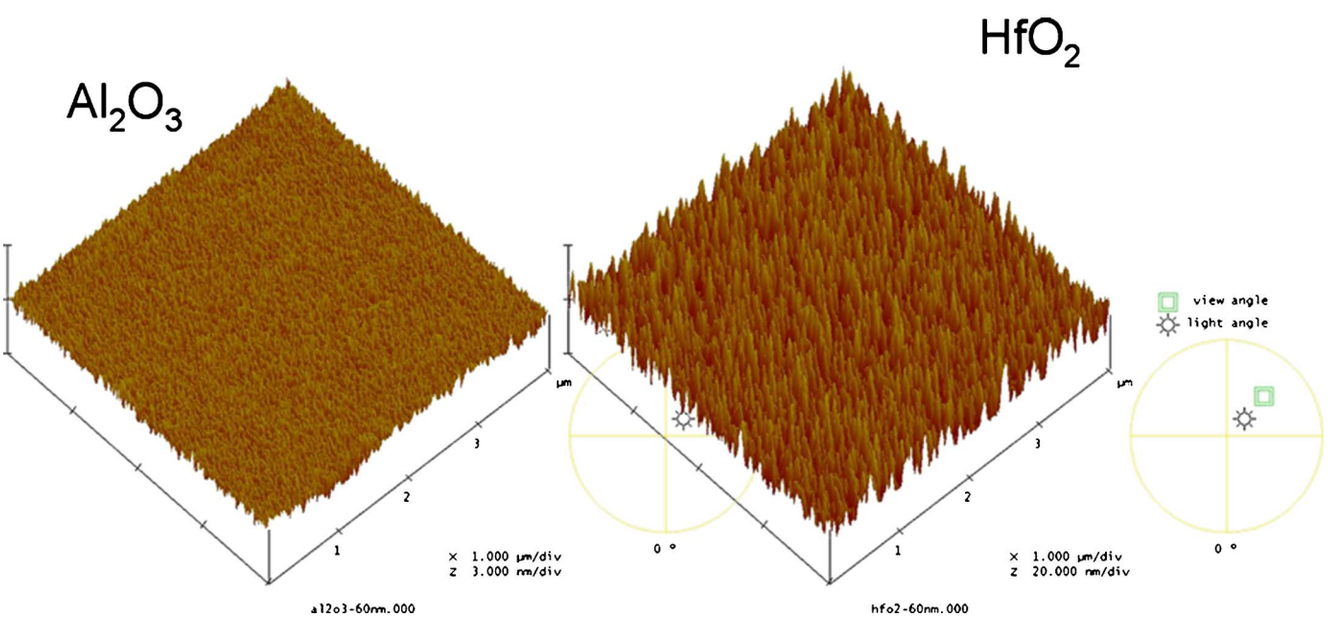

Figure 3. (Color online) 3D AFM images of 60 nm ALD Al_2O_3 and HfO_2 films. The rms roughness of 60 nm Al_2O_3 films is 30 times smoother than the 60 nm HfO_2 films.

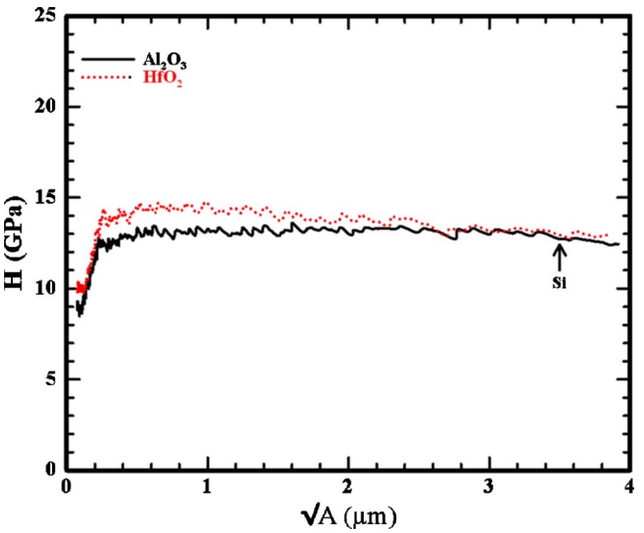

Figure 4. (Color online) Graph showing the 1000 nm indents for 60 nm film thickness of Al_2O_3 and HfO_2.

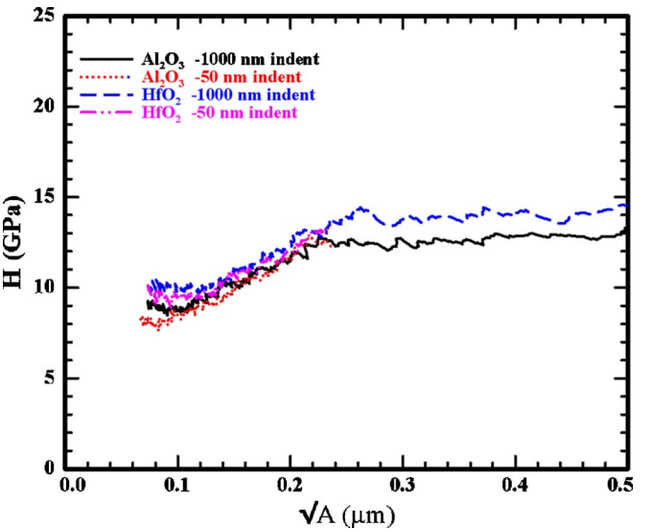

Figure 5. (Color online) Comparison between the 1000 and 50 nm indents for the 60 nm film thickness of Al_2O_3 and HfO_2.

Experimental

Nanoindentation analysis was used to investigate the mechanical properties of ALD Al_2O_3 and HfO_2 thin films. We obtained data from the HfO_2 and Al_2O_3 films in three different steps. In the first step, we only performed indents up to 80% of the top nanolayer film of HfO_2 and Al_2O_3. During the second indentation step, we penetrated through the entire film to the interface, which provides data up to about 100% of the film thickness. Finally, we performed indents up to 1000 nm deep into the bulk Si. For example, for the 60 nm films, a set of shallow indents was made up to 50 nm, which is 80% of the film thickness. Then, another set of indents was made at 60 nm, which is 100% of the film thickness. Finally, a set of indents was made at 1000 nm. The indents were made with a three-sided pyramidal Berkovich tip made of diamond using the continuous stiffness measurement (CSM). The CSM method consists of continuously applying and recording the displacement of the indenter as a function of the applied force during a complete cycle of loading and unloading. Despite the fact that it is redundant to make indents at different depths of indentation because all the desired information i.e., the mechanical properties, can be obtained from one indent performed at a deep depth of indentation with the CSM engaged, we still obtained data at different depths of indentation for comparison and demonstration purposes. In fact, as can be detected from Fig. 4, the 1000 nm indents alone would have been sufficient with the CSM engaged because the hardness can be determined for the surface layers as well as the bulk silicon. From Fig. 5, it is evident that for the 60 nm films of Al_2O_3 and HfO_2 the hardness data from the 1000 and 50 nm indents overlap. In this study, the remainder of the analysis and simulations was performed based on the 1000 nm CSM deep indents. Typical load–depth curves are shown in Fig. 6 and 7. The plots show loading and unloading of an indentation cycle. Figure 6 depicts the 1000 nm indents whereas Fig. 7 demonstrates how the 1000 nm indents overlap the 50 nm indents for both films. During loading, typically the material undergoes elastic and plastic deformation. The peak load during the loading cycle is used to define the hardness. Nanoindentation hardness is defined as the maximum indention load divided by the projected contact area of the indenter tip

$$H = \frac{P_{\max}}{A} \quad [1]$$

where H is the hardness, $P_{\max}$ is the max load, and A is the area of contact.

The hardness measurement critically depends on the area of indentation and the indenter tip calibration. To verify that the areas of indentation were accurately measured and that the indenter tip was appropriately calibrated, we plot in Fig. 8 the contact depth vs the square root of the contact area $\sqrt{A}$ for Al_2O_3 and HfO_2. Data for fused silica calibration standards are shown as well. It is evident that the data of Al_2O_3 and HfO_2 correlate well with each other and with the fused calibration standards. Therefore, we conclude that the areas of indentation measurements are accurate and that the hardness calculations are accurate as well.

The unloading cycle was mainly dominated by elastic displacement. Therefore, the modulus can be obtained from the unloading curve. The elastic modulus was obtained by dividing the slope of the load vs displacement curve at the maximum load data point by the projected contact area of the indenter tip

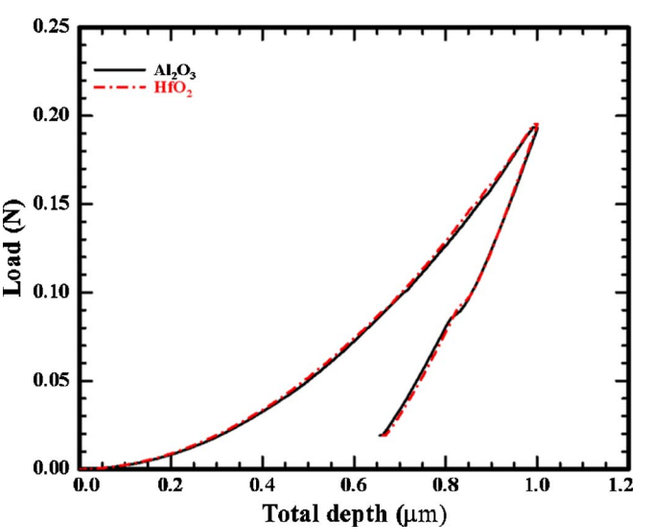

Figure 6. (Color online) Load vs depth showing the loading and unloading mode for 1000 nm deep indents.

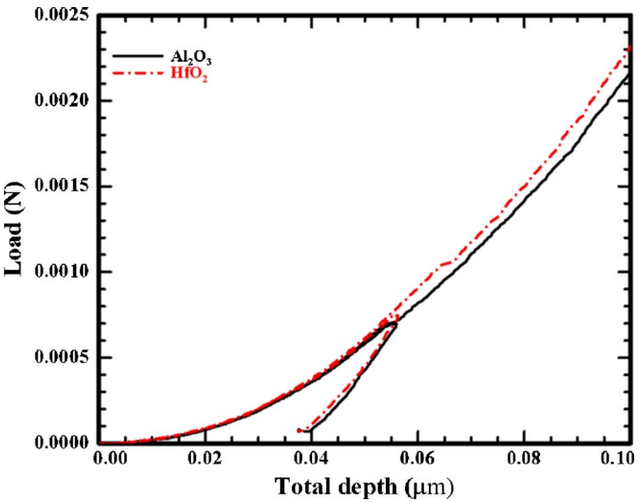

Figure 7. (Color online) Load vs depth for 50 and 1000 nm indents. The 1000 nm profile overlaps the 50 nm one.

$$E = \frac{1}{\beta^* \sqrt{A}} \frac{dP}{dh} \quad [2]$$

where E is the reduced modulus of the specimen, A is the area of contact, dP/dh is the slope of the load–depth curve, and β is a constant depending on both the indenter geometry and Poisson's ratio.

The effective modulus of the specimen is discussed later and the definition of E_{eff} is provided in Eq. 3. The nanoindentation stiffness of the composite HfO_2/Si and Al_2O_3/Si systems was modeled using elasticity theory for indentation against a layered specimen, which will be discussed later.[14] However, during the indentation of some materials, fracture events or debonding at the film–substrate interface may occur and can be observed as discontinuities in the load vs displacement curves. In Fig. 9, AFM micrographs of an indent made by a Berkovich diamond tip on the 104 and 296 Å HfO_2 films show evidence of cracks. We have also noticed that, in the immediate vicinity of the indent, the material that was displaced by the indenter

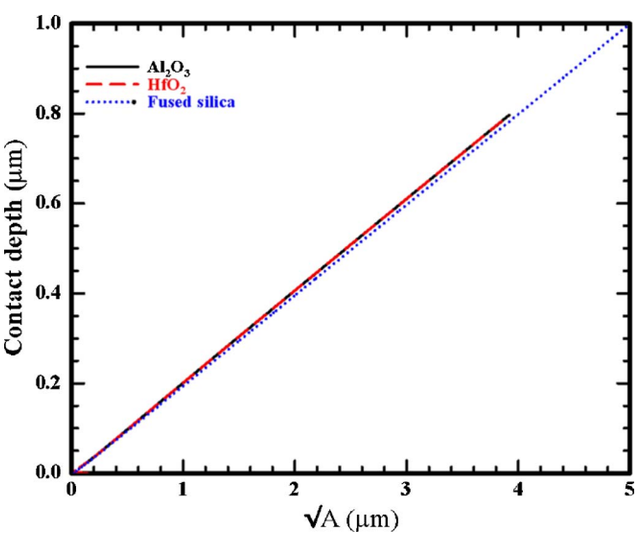

Figure 8. (Color online) Contact depth of indentation vs $\sqrt{A}$. Data for fused silica calibration standards are shown as well.

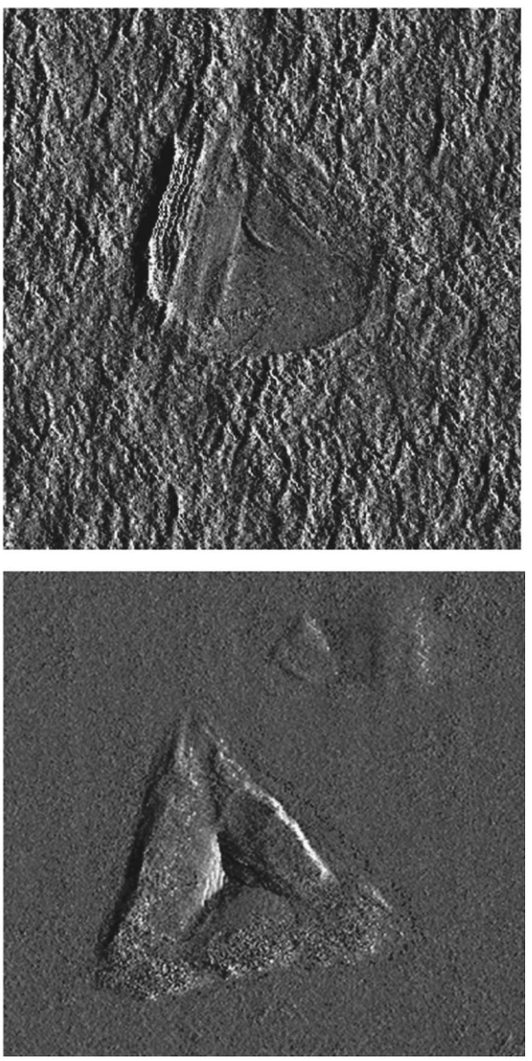

Figure 9. AFM picture of a Berkovich indent that was done on (top) 296 Å HfO_2 and (bottom) 104 Å HfO_2 thin films. The increase in roughness with film thickness can be seen.

is pushed up along the sides of the indenter, similar to a snow plough effect. An example of that phenomenon can be seen in the 104 Å HfO_2 in Fig. 9.

Results and Discussion

In this section, a detailed discussion pertaining to the 1000 nm CSM indents will be presented, which includes all the information of interest from the film surface to the bulk Si underneath. Also, values calculated from individual indents performed by a Hysitron (Minneapolis, MN) Triboindenter with areas measured from AFM images were compared to the values obtained from CSM data. In nanoindentation, the presence of the substrate introduces biases in the measurement of the modulus and hardness of thin films. As the indentation depth gets closer to the interface between the thin film and the substrate, the effect of the substrate becomes more pronounced. One way of reducing the effect of the substrate on the mechanical properties of the high-k dielectric thin films is to model the whole system and perform some data fitting when the substrate properties are known.[14] To take into account the substrate effect, simulations, and modeling based on areas from the AFM images, the substrate properties and the specimen compliance were performed. Figure 10 shows the plot of the normalized compliance and the area

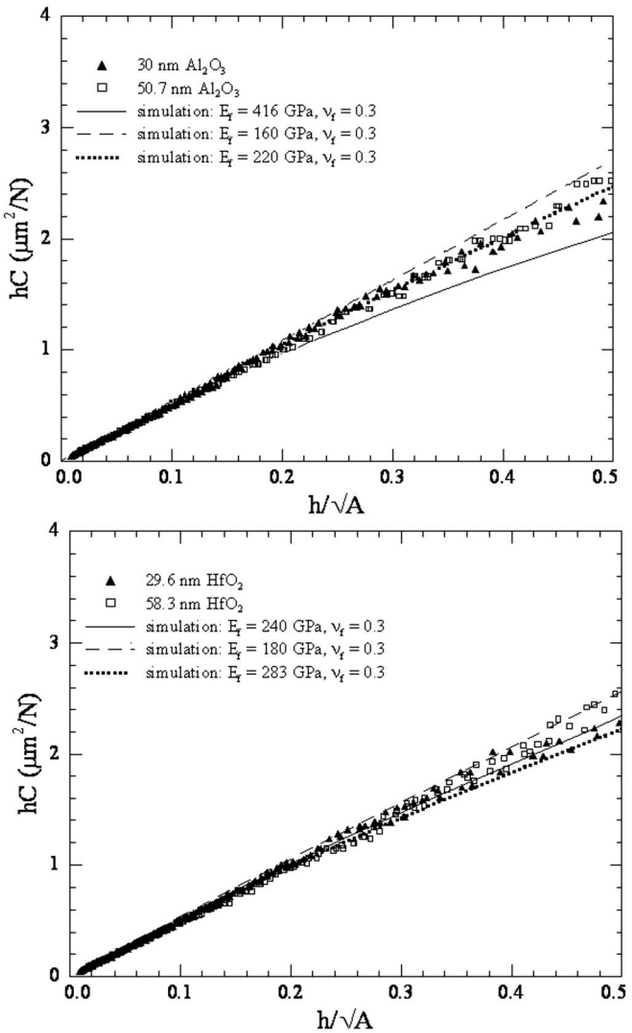

Figure 10. Compliance vs normalized area plot for (top) Al_2O_3 and (bottom) HfO_2 films. H = film thickness, A = area, and C = compliance.

by the film thickness. Comparing the slope of the compliance vs area plot to the simulations allows us to determine the modulus of the film.[14] Figure 11 shows the modulus of Al_2O_3 films vs normalized square root of the area by the film thickness. The data represent the CSM measurement, with individual indents from the Hysitron indenter, and the simulated moduli based on the area measured by AFM.[14] The effective modulus E_{eff} from Fig. 11 was obtained from the simulations and is modeled as follows

$$E_{\text{eff}} = \frac{S}{\sqrt{A}} = \left(\beta\left[\frac{1-\nu_s^2}{E_s} + \frac{1-\nu_i^2}{E_i}\right]^{-1}\right) \qquad [3]$$

for a monolithic specimen, where β is a constant and for this simulation β = 1.22, ν_s = substrate Poisson's ratio, ν_i = indenter Poisson's ratio, E_s = substrate Young's modulus, and E_i = indenter Young's modulus (in this case the Berkovich indenter tip is made of diamond).

From Fig. 10 and 11, the modulus of Al_2O_3 films corresponds to 220 ± 40 GPa. CSM data also correlate well with the individual indents from the Hysitron indenter except for shallow indents. However, there is a weak correlation for very shallow indents. We believe this is due to error and uncertainty in the measured area of the shallow indents. In Fig. 12, the plot of hardness vs the normalized square root of the area is shown. The hardness of Al_2O_3 is

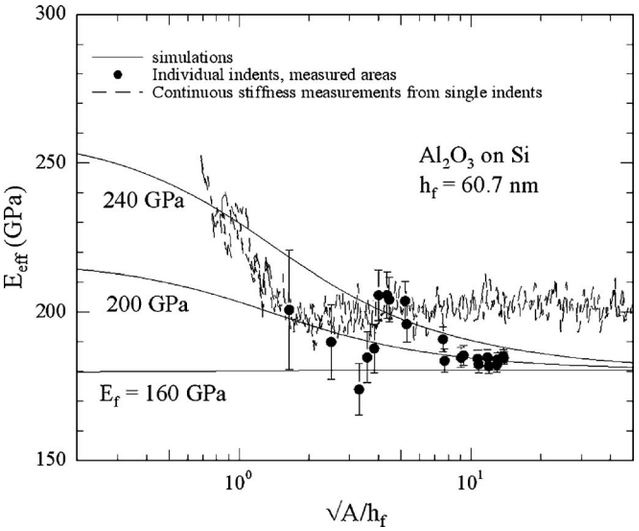

Figure 11. Graph shows the modulus vs normalized square root of the area of contact by film thickness. Modulus of Al_2O_3 is about 220 ± 40 GPa. E_{eff} = film modulus, h_f = film thickness, and A = area of the indent. The error bars are based on the uncertainty of 10 nm of $\sqrt{A}$.

10.5 ± 2 GPa. From the individual indent data for both modulus and hardness in Fig. 11 and 12, a decrease in hardness and modulus is observed at a normalized squared root of the area value of 4–5. This corresponds to an observation that all the indents performed on this 60 nm Al_2O_3 film had a discontinuity in the load vs displacement curves, likely a fracture event, which corresponds to a load of 1 mN. This fracture event most likely influenced the calculated values of modulus and hardness. Figure 13 shows a high-resolution AFM micrograph of the Berkovich indenter tip into the 10 and 30 nm films of Al_2O_3 film, demonstrating the smooth surface morphology and absence of cracks.

Similar results and analysis were obtained for the 60 nm HfO_2 film. The modulus of HfO_2 films is 220 ± 40 GPa and the hardness is 9.5 ± 2 GPa, respectively. Hardness and modulus data of the

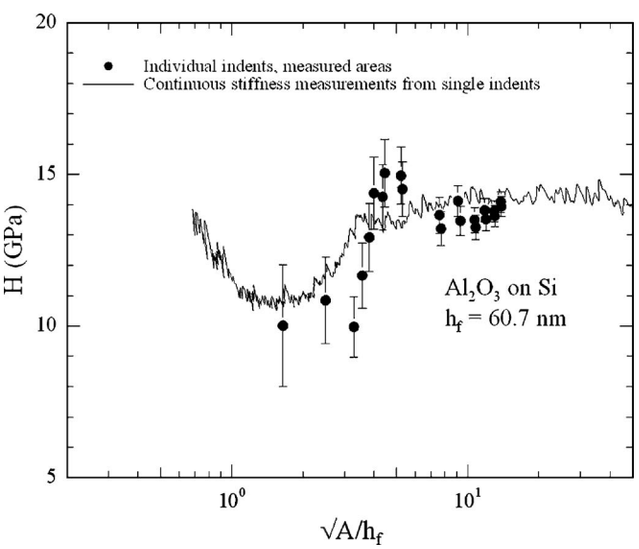

Figure 12. Graph shows the hardness vs normalized square root of the area of contact by film thickness. Hardness of Al_2O_3 is about 10.5 ± 1 GPa. H = film hardness, h_f = film thickness, and A = area of the indent. The error bars are based on the uncertainty of 10 nm of $\sqrt{A}$.

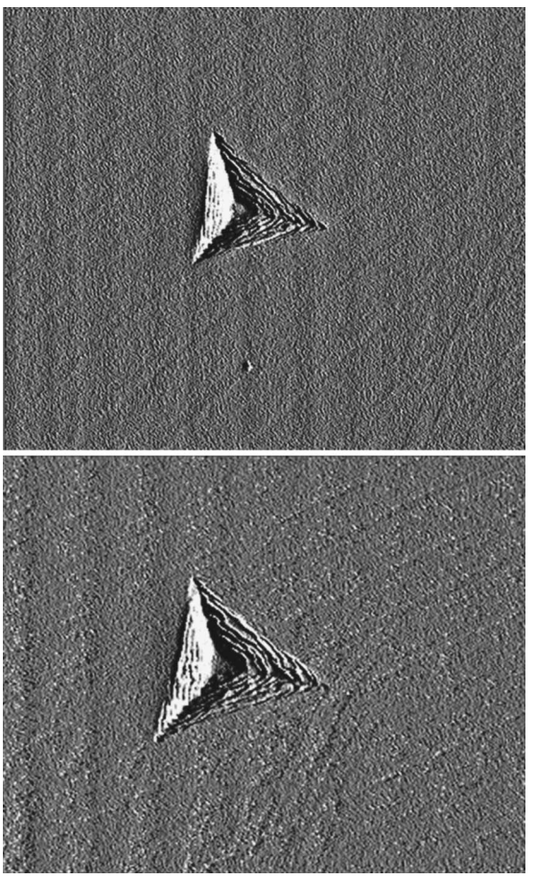

Figure 13. The top picture is an AFM micrograph of a 3.4 mN indent on a 300 Å thick Al_2O_3 thin film; the bottom picture is an AFM micrograph of a 103 Å thick Al_2O_3 thin film demonstrating very smooth surface morphology and absence of defects and cracks. This is in direct contrast with HfO_2 films, where many microcracks were detected.

HfO_2 exhibit more scattering compared to the Al_2O_3 data. This is due to the significantly higher surface roughness of the HfO_2 film. At the constant deposition temperature of 250°C the rms surface roughness of HfO_2 films is approximately a factor of 30 higher than Al_2O_3. These surface features correspond to 5.5% of the HfO_2 film thickness. In contrast, a purely amorphous HfO_2, which was grown one atomic layer at a time by ALD at lower temperatures, would exhibit a very smooth surface morphology. In our case the AFM observed surface roughening of HfO_2 at 250°C provides experimental evidence of the onset of nucleation and growth of crystallites. Each ALD growth cycle produces nucleation sites in a random fashion over the amorphous layers of the growing HfO_2 film. Random nucleation and thermally activated growth of small crystallites are the primary causes of surface roughening in the initially amorphous HfO_2 films.[15] Grain growth of individual crystallites in the amorphous matrix is temperature activated. We have verified that we can obtain purely amorphous HfO_2 films with a very smooth surface morphology by lowering the ALD temperature below 150°C. It is a well-established fact that grain growth occurs at different speeds for different crystallographic orientations. The random orientation of the HfO_2 crystallites embedded in the amorphous matrix guarantees that a sufficient number of HfO_2 crystallites happen to be oriented in such a way that their maximum growth velocity is in the vertical direction. This explains the bumps and surface roughening in ALD HfO_2 films observed by our AFM measurements. It takes well over 600°C to achieve a complete phase change to a 100% polycrystalline HfO_2 film. At our deposition temperature of 250°C we have a fraction of the HfO_2 film crystallized in small grains, which are embedded in the amorphous matrix. From Fig. 9 cracks are observed around the indent on 30 and 10 nm HfO_2 thin films. We attribute the formation of the cracks to the porous, nondensified nature of the amorphous high-*k* films in this study. Because the films used were as-deposited, they incorporate a portion of the deposition gases, for example the carrier gas N_2 in our case. Furthermore, debonding at the interface and microcracks contributed to the growth of the major cracks observed in the films. Microcracks are clearly delineated in the HfO_2 film displaced by the Berkovich indent as seen in Fig. 14. Further studies will be performed in the near future to investigate the reason for the cracks of the films after indentation, to study the

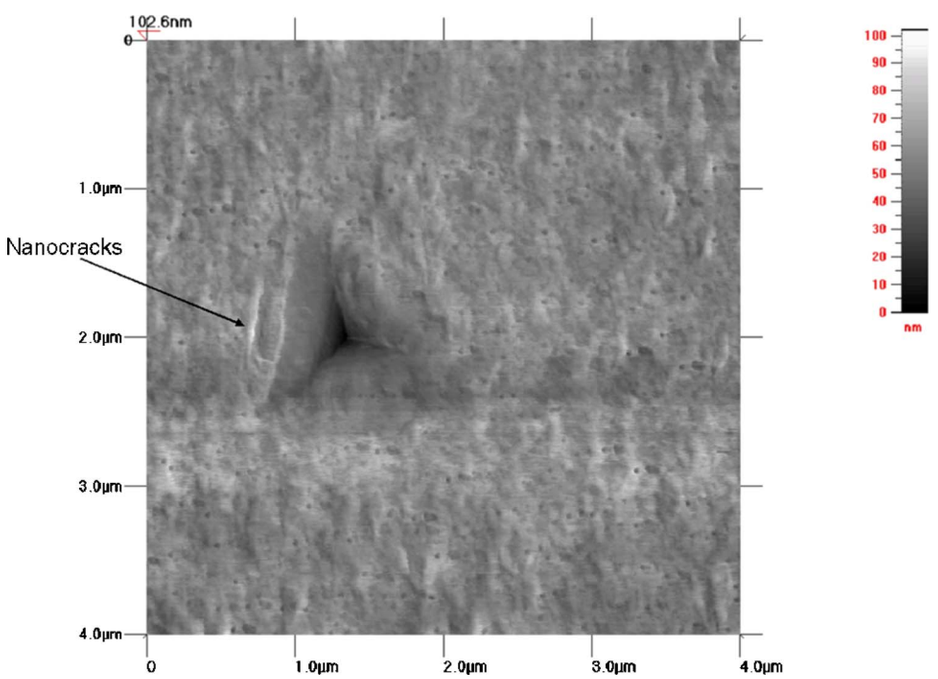

Figure 14. (Color online) The picture shows a 1.5 mN indent in the 10 nm HfO_2 film with a large amount of bubbling up around the indent. The three diamond-shaped objects surrounding the indent represent the inverse shape of the AFM tip, an artifact likely caused by an extremely sharp point present on the surface of the thin film.

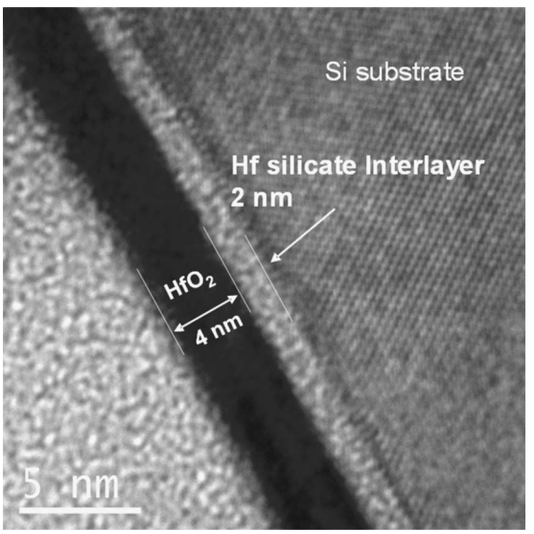

Figure 15. High-resolution TEM cross section of 4 nm HfO_2 film on silicon showing an interlayer of hafnium silicate of about 2 nm.

effect of rapid thermal annealing at higher temperatures on the nanomechanical properties, and to compare the annealed samples to the as-deposited.

The data obtained in this study demonstrate that the hardness results of ALD Al_2O_3 and HfO_2 films are roughly comparable within the accuracy of the indenter measurements.[16] According to the plots of Fig. 4 and 5 there is hardly a difference between the experimental hardness values for both films up to a depth of 50 nm. Once the indenter tip approaches the films' thickness at the interface where the substrate effect becomes significant, the hardness values of both films experience slight changes. HfO_2 instantly becomes harder than Al_2O_3 and remains harder until the indenter tip reaches a depth of 500 nm, where the hardness of both films ultimately converges to the hardness of the bulk Si. However, during deposition of the HfO_2 film on the Si substrate a 2–3 nm thick hafnium silicate interlayer develops at the interface due to the interdiffusion, as depicted by Fig. 15. The interlayer grows thicker for 60 nm HfO_2 film. This hafnium silicate interlayer produces a harder surface directly at the Si interface. The presence of a harder hafnium silicate interlayer combined with poorer adhesion accounts for the transient increase of the hardness for HfO_2 films as shown in Fig. 4 and 5. Al_2O_3 has not experienced this temporary increase in the hardness due to the absence of such an interface layer and due to better substrate bonding conditions. The modulus and hardness values of ALD Al_2O_3 thin films are comparable with literature values. See Table II for details. Little is known about HfO_2 thin films. Finally, Table II summarizes the modulus and hardness of Al_2O_3, HfO_2, and bulk Si from this work and literature values for hardness and modulus deposited with different deposition techniques.

Conclusion

High-k dielectrics are expected to replace SiO_2, SiO_xN_y, and Si_3N_4 as metal-oxide-semiconductor field-effect transistor gate dielectrics or dynamic random access memory (DRAM) memory capacitor dielectrics at the 45 nm technology node and beyond. HfO_2 and Al_2O_3 have attracted attention as potential candidates to find applications as CMOS gate or DRAM capacitor dielectrics. The goal of this study was to focus on the nanomechanical properties of thin films of HfO_2 and Al_2O_3 deposited by ALD. The nanoindentation method was used in conjunction with the CSM method to measure the hardness and modulus. Finally, by combining computer simulations with nanoindentation experimental results for ALD HfO_2 thin films we obtain a hardness of 9.5 ± 2 GPa and a modulus of 220 ± 40 GPa, whereas ALD Al_2O_3 thin films yield a hardness and modulus of 10.5 ± 2 and 220 ± 40 GPa, respectively. Our studies revealed the formation of a much harder 2–3 nm hafnium silicate interlayer, which is responsible for the increase in HfO_2 hardness close to the Si substrate interface. This is in contrast to Al_2O_3, where no such interlayer is found. Further studies will be performed to investigate the root cause for observed defects such as cracks, bubbling of the films, and pop-ins.

Table II. Summary of the measured nanomechanical properties of HfO_2 and Al_2O_3 ALD films.

Thin film	Modulus (GPa)	Hardness (GPa)
HfO_2	220 ± 40	9.5 ± 1
Al_2O_3	220 ± 40	10.5 ± 1
Bulk Si	180 ± 40	13 ± 1
	Literature values for comparison	
Al_2O_3 [a]	180 ± 8.2	12 ± 1
Al_2O_3 [b]	150	9.5
Al_2O_3 [c]	177	9.6
Al_2O_3 [d]	160–180	

[a] Al_2O_3: ALD Al_2O_3 deposited at 177°C.[17]
[b] Al_2O_3: Al_2O_3 deposited by physical vapor deposition.[18]
[c] Al_2O_3: Al_2O_3 deposited by electron cyclotron resonance plasma.[19]
[d] Al_2O_3: Al_2O_3 deposited by evaporation.[20]

Old Dominion University assisted in meeting the publication costs of this article.

References

1. N. Miller, K. Tapily, H. Baumgart, A. A. Elmustafa, G. Celler, and F. Brunier, *Mater. Res. Soc. Symp. Proc.*, **1021E**, 5 (2007).
2. K. Cherkaoui, A. Negara, S. McDonnell, G. Hughes, M. Modreanu and P. K. Hurley, in Proceedings of the 25th International Conference on Microelectronics, Belgrade, Serbia, and Montenegro, p. 351 (2006).
3. S. K. Dey, A. Das, M. Tsai, D. Gu, M. Floyd, R. W. Carpenter, H. D. Waard, C. Werkhoven, and S. Marcus, *J. Appl. Phys.*, **95**, 5042 (2004).
4. C. Dubourdieu, H. Roussel, C. Jimenez, M. Audier, J. P. Senateur, S. Lhostis, L. Auvray, F. Ducroquet, B. J. O'Sullivan, P. K. Hurley, et al. *Mater. Sci. Eng., B*, **118**, 105 (2005).
5. A. C. Jones, H. C. Aspinall, P. R. Chalker, R. J. Potter, K. Kukli, A. Rahtu, M. Ritala, and M. Leskela, *Mater. Sci. Eng., B*, **118**, 97 (2005).
6. D. H. Triyoso, M. Ramon, R. I. Hegde, D. Roan, R. Garcia, J. Baker, X. D. Wang, P. Fejes, B. E. White, and P. J. Tobin, *J. Electrochem. Soc.*, **152**, G203 (2005).
7. H. Ikeda, S. Goto, K. Honda, M. Sakashita, A. Sakai, S. Zaima, and Y. Yasuda, *Jpn. J. Appl. Phys., Part 1*, **41**, 2476 (2002).
8. J. S. Becker, Ph.D. Thesis, Harvard University, Cambridge, MA (2002).
9. W. Deweerd, A. Delabie, S. V. Elshocht, S. D. Gendt, M. Caymax, and M. Heyns, *Future Fab Intl.*, **20**, 93 (2006).
10. S. J. Lee, Y. M. Jung, S. J. Lim, K. H. Lee, S. K. Lee, and T. W. Seo, *J. Appl. Phys.*, **92**, 2807 (2002).
11. M. F. Doerner and W. D. Nix, *J. Mater. Res.*, **1**, 601 (1986).
12. A. C. Fischer-Cripps, *Nanoindentation*, p. 21, Springer-Verlag, Berlin (2002).
13. W. C. Oliver and G. M. Pharr, *J. Mater. Res.*, **7**, 1564 (1992).
14. D. S. Stone, *J. Mater. Res.*, **13**, 3207 (1998).
15. D. M. Hausmann and R. G. Gordon, *J. Cryst. Growth*, **249**, 251 (2003).
16. K. Tapily, J. Jakes, D. S. Stone, P. Shrestha, D. Gu, H. Baumgart, and A. A. Elmustafa, *ECS Trans.*, **11**(7), 123 (2007).
17. M. K. Tripp, C. Stampfer, D. C. Miller, T. Helbling, C. F. Herrmann, C. Hierold, K. Gall, S. M. George, and V. M. Bright, *Sens. Actuators, A* **A130–131**, 419 (2006).
18. T. C. Chou, T. G. Neih, S. D. McAdams, and G. M. Pharr, *Scr. Metall. Mater.*, **25**, 2203 (1991).
19. J. C. Barbour, J. A. Knapp, D. M. Follsteadt, T. M. Mayer, K. G. Minor, and D. L. Linam, *Nucl. Instrum. Methods Phys. Res. B* **166–167**, 140 (2000).
20. N. G. Chechenin, J. Bottiger, and J. P. Krog, *Thin Solid Films*, **304**, 70 (1997).